Supplemental Material

to "Nonhelical inverse transfer of a decaying turbulent magnetic field" (arXiv:1404.2238)

by A. Brandenburg, T. Kahniashvili, & A. G. Tevzadze

The focus of the accompanying Letter is the investigation of inverse transfer of magnetic energy at the expense of kinetic energy at intermediate scales. In this Supplemental Material, we present additional details of the resulting turbulence regarding initial conditions, decay rate, the mechanisms for inverse transfer, including the question of local two-dimensionality of the turbulence, and the spectral energy transfer functions.

INITIAL CONDITION

Initial conditions can be obtained either as a result of an earlier turbulence simulation driven by monochromatic driving or the fields can be synthesized with given power spectra and random phases. In the following, we describe and compare these cases.

Via monochromatic driving

Our goal is to have an initial condition that quickly leads to self-similar decay. Earlier experience [1] has shown that this is easily achieved by using a snapshot from a turbulence simulation that was driven with stochastic monochromatic forcing in the equation for the magnetic vector potential. The resulting initial condition used in our present work is shown in Figure 1. It shows approximate k^2 and k^4 subinertial ranges for kinetic and magnetic energy spectra, respectively. The initial energies are $\mathcal{E}_{\rm M}(0)=v_{\rm A0}^2/2$ and $\mathcal{E}_{\rm K}(0)=u_0^2/2$ with $v_{\rm A0}=0.15$ and $u_0=0.10$. Both spectra are maintained also at later times in such a way that they gradually shift with time (see Fig. 1 of the Letter).

In the present simulations (Run A of the Letter), both magnetic and kinetic energies show a slight uprise of power near the Nyquist wavenumber, $k_{\rm Ny}=\pi/\delta x$, where δx is the mesh spacing. This indicates that the resolution is only marginal for the Reynolds number chosen here. However, during the subsequent decay calculation, after several Alfvén times, this excess power at $k_{\rm Ny}$ disappears, as is seen in Fig. 1 of the Letter.

Via random phases

An alternative mechanism of producing initial conditions is to generate a vector field in wavenumber space with a given spectrum and random phases. In Figure 2 we show an example where we have for magnetic energy

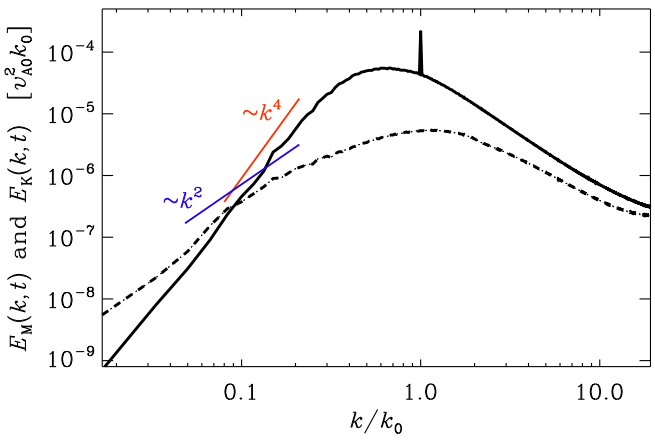

FIG. 1: Magnetic (solid lines) and kinetic (dashed lines) energy spectra for the initial condition of Run A.

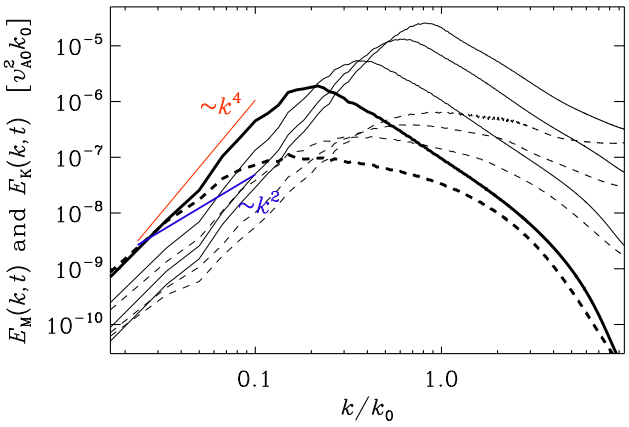

FIG. 2: Like Figure 1, but with an initial k^4 spectrum for magnetic energy using random phases;

a k^4 spectrum for $k<k_0$ and $k^{-5/3}$ for $k>k_0$, but zero kinetic energy ($v_{\rm A0}=0.40$ and $u_0=0$). Our initial velocity is zero and the initial vector potential in Fourier space is $\hat{A}_j(\boldsymbol{k})$ such that for all three components j are given by

$$k\hat{A}_j(\boldsymbol{k})=A_0\frac{(k/k_0)^{n_1/4-1/2}}{[1+(k/k_0)^{n_1-n_2}]^{1/4}}\,e^{{\rm i}\phi(\boldsymbol{k})}, \qquad (1)$$

where $n_1=4$ and $n_2=-5/3$ are the exponents of the related magnetic energy spectrum, $\phi(\boldsymbol{k})$ are random phases, A_0 is the amplitude, and $k=|\boldsymbol{k}|$. We choose $k_0/k_1=60$ and run with $\nu=5\times10^{-6}$ at 1152^3 meshpoints, which is slightly more dissipative than the runs reported in the Letter with $\nu=2\times10^{-6}$ using 2304^3 meshpoints. In Figure 2 we show the times $t/\tau_{\rm A}=10$, 50, 200, and 900, where $\tau_{\rm A}=(v_{\rm A0}k_0)^{-1}\approx0.042$ is the initial Alfvén time.

At very early times ($t\approx\tau_{\rm A}$), a k^4 kinetic energy spectrum develops, which is consistent with the causality con-

straint, but after several hundred Alfvén times the spectrum becomes gradually shallower and approaches a k^2 subinertial range. However, unlike the initial condition shown in Figure 1, the magnetic field is continuously decaying and the integral scale is increasing, which is the reason why the k^2 subinertial range is less strongly developed in Figure 2. Nevertheless, the magnetic spectrum shows again clear inverse transfer, although it is initially somewhat slower, as can be expected given the time it takes to build up the k^2 velocity spectrum.

Steeper initial spectra

If we start with a magnetic energy spectrum steeper than k^4, the spectrum quickly changes into a k^4. This is demonstrated in Figure 3, where we start with an initial k^6 spectrum, followed by a $k^{-5/3}$ subrange. We show the times $t/\tau_A = 1$, 5, 20, 80, and 400, and see that already at $t/\tau_A = 20$ the subinertial range has nearly a k^4 subrange.

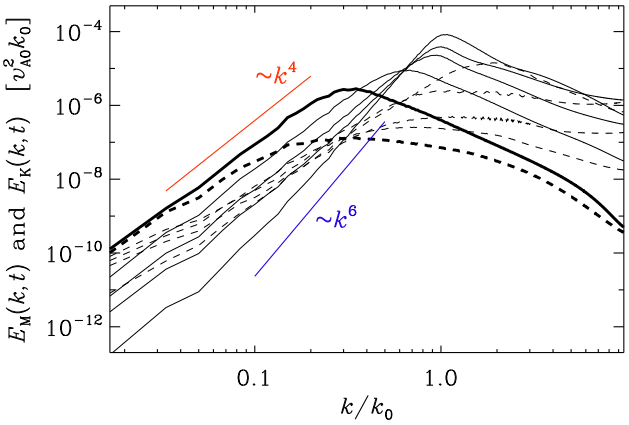

FIG. 3: Like Figure 2, but with an initial k^6 spectrum for the magnetic energy using random phases.

EVOLUTION

Integral scale

The decay of MHD turbulence is characterized by the kinetic and magnetic integral scales. The kinetic integral scale $\xi_K = k_K^{-1}$ is defined analogously to the magnetic one $\xi_M = k_M^{-1}$ (given in the Letter), with

$$k_K^{-1}(t) = \int_0^\infty k^{-1} E_K(k,t)\, dk / \mathcal{E}_K(t). \qquad (2)$$

Both scales grow in time nearly perfectly proportional to each other like $t^{1/2}$; see Figure 4. The corresponding decay of kinetic and magnetic energies is proportional to t^{-1} and is addressed below in this Supplemental Material where we plot $u_{rms} = (2\mathcal{E}_K)^{1/2}$ and $v_A = (2\mathcal{E}_M)^{1/2}$ vs. t.

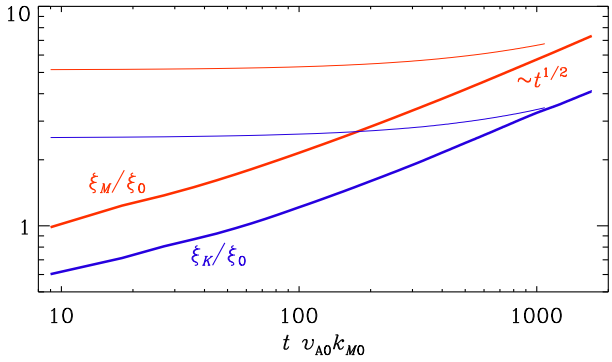

FIG. 4: Kinetic and magnetic integral scales, ξ_K and ξ_M, respectively, for Runs A (thick lines) and B (thin lines).

In Table 1 of Ref. [2], Campanelli has summarized the decay laws for various subinertial range scalings using both helical and non-helical MHD turbulence. The scaling exponent for the magnetic integral scale, $\xi_M = k_M^{-1}(t) = \int k^{-1} E_M(k,t)\, dk / \mathcal{E}_M(t)$, is around 1/2 for most of the cases. It emerges quite generically from scaling arguments first derived by [3]. Kalelkar & Pandit [4] find $\xi_M \sim t^{1/2}$ for an initial spectrum $E_M \sim k$, but the same scaling also emerges for other initial power laws, as has been demonstrated by numerous simulations [1]. The reason for this is that the decay properties depend mainly on nature of the turbulence (being either hydrodynamic, hydromagnetic without helicity, or with helicity).

Mach & Alfvén numbers

In Figure 5, we plot the evolution of the Mach number u_{rms}/c_s, the Alfvén number u_{rms}/v_A, and the ratio v_A/c_s, where u_{rms} and v_A are the rms values of velocity and magnetic field (density is approximately constant), and $c_s = \text{const}$ is the isothermal sound speed.

Both u_{rms} and v_A decay in time proportional to $t^{-1/2}$, so the kinetic and magnetic energies decay like $\mathcal{E}_K(t) = u_{rms}^2/2 \propto t^{-1}$ and $\mathcal{E}_M(t) = v_A^2/2 \propto t^{-1}$. Earlier work [1] resulted in a decay law proportional to $t^{-0.9}$, but this departure from the t^{-1} law is likely a consequence of insufficient scale separation; k_0/k_1 is now 60 compared to 15 previously.

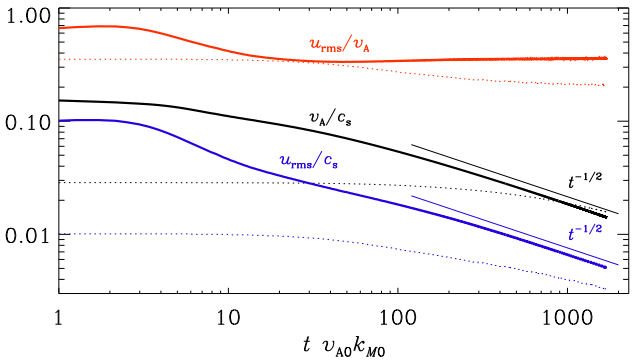

FIG. 5: Mach number $u_{\rm rms}/c_{\rm s}$ (black), Alfvénic Mach number $u_{\rm rms}/v_{\rm A}$ (red), and the ratio $v_{\rm A}/c_{\rm s}$ (blue) for Runs A (thick, solid lines) and B (dotted lines).

Loitsyansky invariant

In hydrodynamic turbulence, using the constancy of the Loitsyansky invariant,

$$\mathcal{L}=\int \boldsymbol{r}^2\langle \boldsymbol{u}(\boldsymbol{x})\cdot\boldsymbol{u}(\boldsymbol{x}+\boldsymbol{r})\rangle\,d\boldsymbol{r}\propto \ell^5 u_\ell^2, \tag{3}$$

with typical velocity u_ℓ on scale ℓ, Kolmogorov argued on dimensional grounds that the kinetic energy should decay like $\mathcal{E}_{\rm K}\propto\mathcal{L}^{2/7}t^{-10/7}$. On the other hand, if the decay is governed by viscosity, dimensional arguments suggest $\mathcal{E}_{\rm K}\propto\nu t^{-1}$ and $\ell\propto(\nu t)^{1/2}$, both of which appear consistent with our simulations. If that is the case, we should expect $\mathcal{L}$ to grow with time like $\mathcal{L}\propto\nu^{5/2}t^{1/2}$.

In Table I we give values of $\mathcal{L}$ and $\langle\boldsymbol{u}^2\rangle$ for a low resolution run (64^3 mesh points) and a down-sampled one of Run A of the Letter (2304^3 mesh points).

TABLE I: Values of $\mathcal{L}$ and $\langle\boldsymbol{u}^2\rangle$ for a low resolution run (64^3 mesh points) and a down-sampled one of Run A of the Letter (2304^3 mesh points).

resol.	t	$\mathcal{L}$	$\langle\boldsymbol{u}^2\rangle$
64^3	40	$+2.1\times10^{-7}$	8.0×10^{-3}
	100	-5.4×10^{-7}	7.0×10^{-5}
	250	-8.4×10^{-7}	1.1×10^{-5}
2304^3	50	-4.4×10^{-9}	1.0×10^{-4}
	150	-1.1×10^{-8}	3.3×10^{-5}

Table I suggests that $|\mathcal{L}|$ has indeed a tendency to increase with time. This would support our argument above in favor of viscously dominated decay behavior. On the other hand, as the resolution is increased by a factor of 36, $\mathcal{L}$ deceases by about two orders of magnitude while $u_{\rm rms}$ stays about the same. This would be consistent with $\mathcal{L}$ converging to zero and therefore not being able to constrain the decay.

Comparison with hydrodynamics

In the absence of magnetic fields, there is purely hydrodynamic decay without the mutual interaction between two energy reservoirs. This leads to a steeper decay law for kinetic energy and a slower growth of the integral scale, as can be easily be verified by applying an initial k^4 spectrum for the kinetic energy. This is shown in Figure 6, where we compare the decay spectra for hydrodynamic turbulence with nonhelical and helical magnetohydrodynamic turbulence.

Scaling behavior

According to the Olesen scaling law [3], both kinetic and magnetic energies should decay like

$$E_{\rm K}(k,t)\sim E_{\rm M}(k,t)\sim k^\alpha\psi(k^{(3+\alpha)/2}t). \tag{4}$$

Integrating over k yields the decay law of the energies as

$$\mathcal{E}_{\rm K}(t)=\int E_{\rm K}(k,t)\,dk\sim\int k^\alpha\psi(k^{(3+\alpha)/2}t)\,dk. \tag{5}$$

Introducing $\kappa=kt^q$ with $q=2/(3+\alpha)$, we have

$$\mathcal{E}_{\rm K}(t)\sim t^p\int\kappa^\alpha\psi(\kappa)\,d\kappa, \tag{6}$$

where $p=(1+\alpha)q$. The integral scales like $k_K\sim t^q$ with $q=2/(3+\alpha)$. Several parameter combinations are given in Table II.

TABLE II: Parameter combinations of $q=2/(3+\alpha)$, $p=2(1-q)$ and $\alpha=2/q-3$. Note that $10/7\approx1.43$ and $2/7=0.286$.

α $(=\beta)$	p	q	physics
4	10/7	2/7	$\mathcal{L}=$ const
3	8/6	2/6	
2	6/5	2/5	
1	4/4	2/4	$\langle\boldsymbol{A}^2_{\rm 2D}\rangle=$ const (?)
0	2/3	2/3	$\langle\boldsymbol{A}\cdot\boldsymbol{B}\rangle=$ const

The numbers in Table II suggest that different subinertial range scalings $\propto k^\alpha$ correspond to different exponents p and q. Instead, we now argue that the subinertial range scaling is not characterized just by α, but mainly by the slope of $\psi(k)$ for small values of k. To demonstrate this, let us begin by noting that, in practice, it is more accurate to relate the change in the amplitude to the change in the correlation length instead of the time, because it always takes a while to establish asymptotic scaling behavior. Therefore, instead of using Equation (4), we prefer

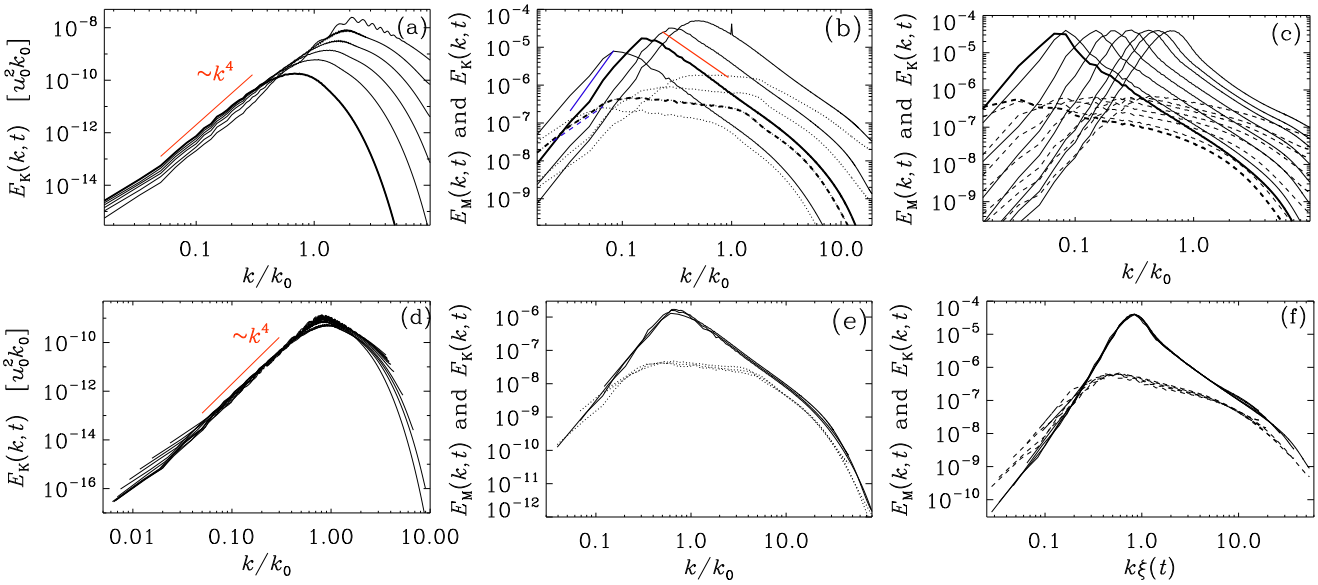

FIG. 6: Kinetic energy spectra in a hydrodynamic simulation (a), compared with magnetic (solid) and kinetic (dashed) energy spectra in a hydromagnetic simulation without helicity (b), and with (c). Panels (d)–(f) show the corresponding collapsed spectra obtained by using $\beta = 3$ (d), $\beta = 1$ (e), and $\beta = 0$ (f).

the following alternative formulation by extracting just a time-dependent factor from the spectrum and write [5]

$$E_{\rm M}(k,t) \sim \xi^{-\beta}\phi(k\xi), \tag{7}$$

with $\xi(t) \sim t^q$ standing either for $\xi_{\rm M}$ (in the magnetic case) or for $\xi_{\rm K}$ (in the hydrodynamic case). The exponent q can be determined by dimensional arguments, e.g. by assuming $\mathcal{L} = \text{const} = U^2 L^5$, which implies

$$\mathcal{L} \sim u^2 l^5 \sim l^7 \tau^{-2} \to q = 2/7,\ p = 10/7\ (\beta = 4). \tag{8}$$

Alternatively, in the presence of helical magnetic fields, $\langle \boldsymbol{A}\cdot\boldsymbol{B}\rangle$ is conserved. Again, from dimensional arguments we find

$$\langle \boldsymbol{A}\cdot\boldsymbol{B}\rangle \sim u^2 l \sim l^3\tau^{-2} \to q = 2/3,\ p = 2/3\ (\beta = 0). \tag{9}$$

Finally, in nonhelical hydromagnetic turbulence we have $q = 1/2$, which suggests that a quantity with the dimensions $u^2 l^2$ should be constant. Since $\langle \boldsymbol{A}^2\rangle/\mu_0\rho_0$ has such dimensions $u^2 l^2$, we must carefully reassess our previous findings suggesting that the flow is fully three-dimensional. Nevertheless, tentatively one can state

$$\langle \boldsymbol{A}_{\rm 2D}^2\rangle \sim u^2 l^2 \sim l^4\tau^{-2} \to q = 1/2,\ p = 1\ (\beta = 1), \tag{10}$$

where $\boldsymbol{A}_{\rm 2D}$ is the gauge that aligns $\boldsymbol{A}$ with the intermediate rate-of-strain vector; see Section . Equations (8)–(10) a decay law $E_{\rm M} \sim t^{-p}$ with $p = (1+\beta)\,q$, where β is a parameter that is usually *not* associated with the subinertial range scaling exponent α. Formally, however, we find that $\alpha = \beta$, so the parameter combinations in Table II still apply with $\alpha = \beta$, but this new formulation does not imply anything about the subinertial range scaling.

INVERSE TRANSFER

The growth of spectral energy at small wavenumbers is cautiously referred to as inverse *transfer*. By contrast, in an inverse *cascade* there is a k-independent flux of some quantity (e.g., magnetic helicity in three-dimensional hydromagnetic turbulence) toward progressively smaller k.

An inverse cascade is known to exist in three dimensional hydromagnetic turbulence if there is helicity. Also two-dimensional hydrodynamic turbulence is known to exhibit inverse cascade behavior. While any of these mechanisms could in principle play a role in explaining the behavior seen in the accompanying Letter, there may also be completely different mechanisms that could potentially explain the growth of spectral magnetic energy at large length scales.

In order to narrow down possible reasons for the inverse transfer found in our simulations, we begin by discussing the concepts of eddy noise and the unwinding of magnetic fields. We also determine the magnetic helicity as well as various other helicities and examine whether the flow could be locally two-dimensional, which might provide yet another cause of inverse transfer, in which case one could appeal to the inverse cascade of $\langle \boldsymbol{A}_{\rm 2D}^2\rangle$, where $\boldsymbol{A}_{\rm 2D}$ is the magnetic vector potential perpendicular in a gauge in which it is locally aligned with the intermediate eigenvector of the rate-of-strain tensor.

Eddy noise

Eddy noise has been mentioned as a mechanism that brings energy from the unresolved scales into resolved scales [6, 7]. The physics of this mechanism is obscured by the fact that it referred originally to numerical artifacts. In particular, it is not obvious that it really leads to a spectral increase of power rather than just a preferential decay at small scales. Of course, at a descriptive level, the concept of eddy noise may be the similar to what we find, although there was never a clear demonstration of the resulting spectral evolution.

Unwinding magnetic fields

One could imagine that the unwinding of a magnetic field leads to the conditions seen in the Letter. Again, this is only a descriptive concept, but one could think of addressing this question through a numerical experiment. Winding up an externally imposed magnetic field leads to magnetic flux expulsion. We now ask about the dynamical behavior of such a magnetic field after the diving force is turned off.

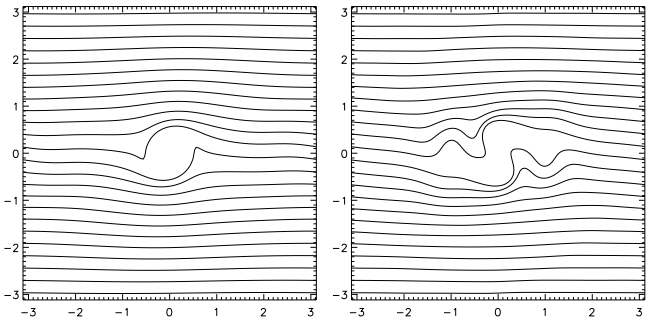

FIG. 7: Field lines in a two-dimensional simulation in the presence of a forced hydromagnetic eddy at an intermediate time (left) and a later time (right) when the eddy has been altered by the Lorentz force in a time-dependent manner.

There are several complications with this seemingly simple idea. First, the original problem of Weiss was not dynamic, but kinematic. Allowing the flow to be a self-consistent solution of the momentum equation leads to more complicated behavior, as demonstrated in Figure 7, where the driving force is given by $\boldsymbol{f} = \boldsymbol{\nabla}\times\psi\hat{\boldsymbol{z}}$ with $\psi = \cos k_1 x \cos k_1 y \exp(-r^2/2R^2)$, and $r^2 = x^2+y^2$. Second, turning off the driving leads to propagating Alfvén waves and long-term oscillations at large scales, which is very different from what is seen in the Letter. However, this behavior can easily be removed by also turning off the imposed magnetic field. Finally, the eddy shown in Figure 7 is too big ($R = 0.1$) and there would be no extended subinertial range. Thus, we now repeat this experiment with a much smaller eddy of radius $R = 0.002$. The resulting spectral evolution is shown in Figure 8.

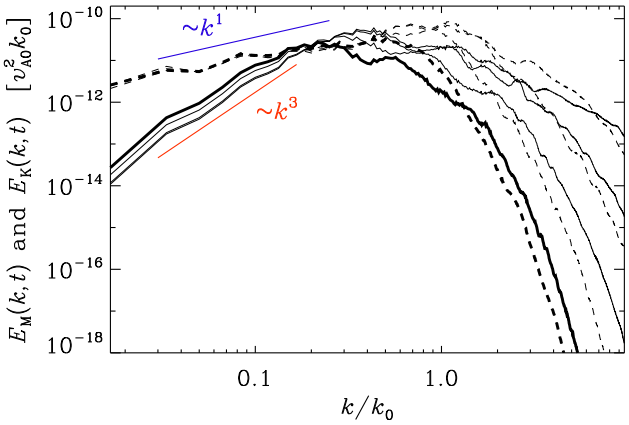

FIG. 8: Kinetic and magnetic energy spectra. The two red lines are proportional to k^1 and t^3, respectively.

In this experiment, the initial magnetic field is a global one and it therefore unconstrained by causality. It turns out that the magnetic energy now has a k^3 subrange at large scales. Interestingly, as the magnetic field decays, there is a slight decay also at large length scales, so there is no inverse transfer in such a setup.

Helicities for Runs A and B

In Table III we list various helicities for Runs A and B. The normalized kinetic helicity $\langle\boldsymbol{\omega}\cdot\boldsymbol{u}\rangle/\omega_{\rm rms}u_{\rm rms}$ and the normalized cross helicity $2\langle\boldsymbol{u}\cdot\boldsymbol{b}\rangle/(u_{\rm rms}^2+b_{\rm rms}^2)$ are less than 0.4%, the normalized current helicity $\langle\boldsymbol{j}\cdot\boldsymbol{b}\rangle/j_{\rm rms}b_{\rm rms}$ is less than 2%, and the normalized magnetic helicity $k_1\langle\boldsymbol{a}\cdot\boldsymbol{b}\rangle/b_{\rm rms}^2$ is less than 1%. In this Letter, it was shown that the level of magnetic helicity was small enough so as not to constrain (i.e., enhance) the growth of the integral scale. Also the other helicities appear to be small enough for being important in explaining the inverse transfer.

TABLE III: Various helicities for Run A of the Letter.

quantity	expression	value
kinetic hel.	$\langle\boldsymbol{\omega}\cdot\boldsymbol{u}\rangle/\omega_{\rm rms}u_{\rm rms}$	0.00364
current hel.	$\langle\boldsymbol{j}\cdot\boldsymbol{b}\rangle/j_{\rm rms}b_{\rm rms}$	0.01693
cross hel.	$2\langle\boldsymbol{u}\cdot\boldsymbol{b}\rangle/(u_{\rm rms}^2+b_{\rm rms}^2)$	−0.00318
magnetic hel.	$k_1\langle\boldsymbol{a}\cdot\boldsymbol{b}\rangle/b_{\rm rms}^2$	0.00976

Projections onto strain tensor

To examine whether there is a tendency for the turbulence to become locally two-dimensional, we compute the rate-of-strain tensor,

$$s_{ij} = \tfrac{1}{2}\left(u_{i,j} + u_{j,i}\right). \tag{11}$$

Since s_{ij} is symmetric, it has three real eigenvalues, λ_i for $i = 1$, 2, and 3. They are traditionally ordered such that

$$\lambda_1 < \lambda_2 < \lambda_3. \tag{12}$$

The corresponding eigenvectors are called $\hat{\boldsymbol{e}}_i$.

If the flow was incompressible, their sum would vanish, which is here also approximately the case. The largest eigenvalue λ_3 corresponds to stretching in the direction $\hat{\boldsymbol{e}}_3$, and the most negative one, λ_1, corresponds to compression in the direction $\hat{\boldsymbol{e}}_1$.

It has been known for some time that in isotropic turbulence the vorticity vector tends to be aligned with the direction $\hat{\boldsymbol{e}}_2$ and is therefore normal to the plane where the flow would be two-dimensional. If the turbulence was perfectly two-dimensional, the intermediate eigenvalue of the rate-of-strain tensor would vanish. This is however not the case; see Figure 9, where we plot probability density functions (PDFs) of the three eigenvalues.

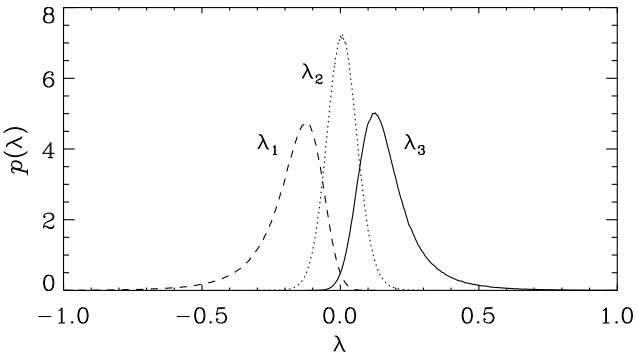

FIG. 9: PDF of the eigenvalues of the rate-of-strain tensor. Note that the intermediate ones are not vanishing, as expected for two-dimensional turbulence.

In the present simulations, we see all the usual characteristics of three-dimensional MHD turbulence where the vorticity vector $\boldsymbol{\omega}$ is aligned with the eigenvector $\hat{\boldsymbol{e}}_2$. Also the magnetic field $\boldsymbol{B}$ is aligned with $\hat{\boldsymbol{e}}_2$; see Figure 10. Here, the PDFs $p(\cos\phi)$ are normalized such that

$$\int_0^1 p(\cos\phi)\, d\cos\phi = 1. \tag{13}$$

Furthermore, while $\boldsymbol{\omega}$ is perpendicular to $\hat{\boldsymbol{e}}_1$ and $\hat{\boldsymbol{e}}_3$, the angle between $\boldsymbol{B}$ and both $\hat{\boldsymbol{e}}_1$ and $\hat{\boldsymbol{e}}_3$ is about 45° (see lower panel of Figure 10), which was first found in MHD shear flows; see Ref. [8], who interpreted their finding as alignment with the direction of the overall shear. We recall that a shear flow can be decomposed into a rotational and a straining motion [9]. The rotational motion is not captured by the strain tensor. The directions of compression and stretching are then at 45° angles with respect to the direction of the shear [10]. Similar results have recently also been obtained in Ref. [11].

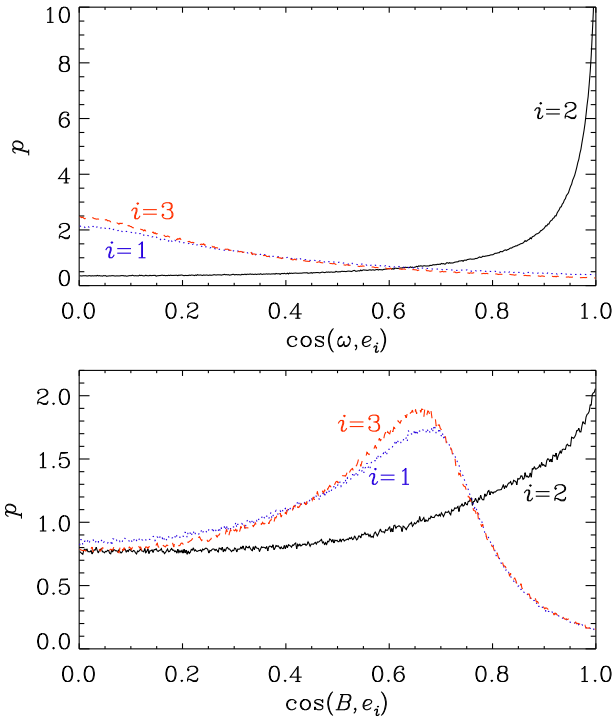

FIG. 10: Alignment of $\boldsymbol{\omega}$ and $\boldsymbol{B}$ with the eigenvectors of the rate-of-strain tensor.

Next, we compute the projections of various vectors $\boldsymbol{\sigma}$ onto s_{ij}:

$$\mathsf{s}_\sigma = \langle \sigma_i s_{ij} \sigma_j \rangle / \langle \boldsymbol{\sigma}^2 \rangle, \tag{14}$$

where $\boldsymbol{\sigma}$ stands for either $\boldsymbol{u}$, $\boldsymbol{\omega}$, $\boldsymbol{B}$, or $\boldsymbol{J}$. For $\boldsymbol{\omega}$ and $\boldsymbol{B}$, these values quantify the production of $\boldsymbol{\omega}$ and $\boldsymbol{B}$, respectively, but for the other quantities no such interpretation exists. In Table IV we give the mean and rms values of the s_σ. Here we also compare with the projection of $\boldsymbol{A}$ onto the direction $\hat{\boldsymbol{e}}_2$, i.e., $\boldsymbol{A} \to \hat{\boldsymbol{e}}_2(\boldsymbol{A}\cdot\hat{\boldsymbol{e}}_2)$, and therefore $\mathsf{s}_A = \langle \lambda_2 (\boldsymbol{A}\cdot\hat{\boldsymbol{e}}_2)^2 \rangle / \langle (\boldsymbol{A}\cdot\hat{\boldsymbol{e}}_2)^2 \rangle$.

Note that s_A is not particularly small, as one would have expected for a locally nearly two-dimensional flow and is comparable to all the other terms. The average of $\langle B_i s_{ij} B_j \rangle / \langle \boldsymbol{B}^2 \rangle$ is actually the smallest one among them all.

TABLE IV: Mean and rms values of the normalized projections s_σ with $\boldsymbol{\sigma} = \boldsymbol{u}$, $\boldsymbol{\omega}$, $\boldsymbol{B}$, and $\boldsymbol{J}$ onto s_{ij} and a comparison with the value of s_A defined in the text.

$\boldsymbol{\sigma}$	$\boldsymbol{u}$	$\boldsymbol{\omega}$	$\boldsymbol{B}$	$\boldsymbol{J}$	$\boldsymbol{A}$
mean	0.009	0.019	−0.001	0.005	0.007
rms	0.145	0.204	0.069	0.064	0.106

Conservation of squared potential?

In the Letter, we have argued that the inverse transfer can be a consequence of the different subinertial range scalings for kinetic and magnetic energy spectra. However, as a very different possibility we also have to consider an inverse cascade due to the approximate invariance of $\langle \boldsymbol{A}^2 \rangle$ in two dimensions [12]. This would seem surprising given the similar widths of the PDFs of the intermediate eigenvalue λ_2 and those of λ_1 and λ_3, which suggests that the flow cannot be regarded as locally two-dimensional.

The quantity $\langle \boldsymbol{A}^2 \rangle$ is obviously gauge-dependent. However, the relevant gauge is one that aligns $\boldsymbol{A}$ locally with $\hat{\boldsymbol{e}}_2$. Thus, we use the new vector potential

$$\boldsymbol{A}_{\rm 2D} = \boldsymbol{A} + \boldsymbol{\nabla}\Lambda, \tag{15}$$

such that

$$0 = \hat{\boldsymbol{e}}_2 \times \boldsymbol{A} + \hat{\boldsymbol{e}}_2 \times \boldsymbol{\nabla}\Lambda. \tag{16}$$

Taking the curl yields

$$0 = \hat{\boldsymbol{e}}_2 \cdot \boldsymbol{\nabla} \times (\hat{\boldsymbol{e}}_2 \times \boldsymbol{A}) + \hat{\boldsymbol{e}}_2 \cdot \boldsymbol{\nabla} \times (\hat{\boldsymbol{e}}_2 \times \boldsymbol{\nabla}\Lambda). \tag{17}$$

We define $\tilde{\boldsymbol{A}}(\boldsymbol{k},t) = \int \boldsymbol{A}(\boldsymbol{x},t)\, e^{-i\boldsymbol{k}\cdot\boldsymbol{x}}\, d^3x$ as the Fourier transformed vector potential to obtain

$$\boldsymbol{\nabla}\Lambda = -\int \frac{\boldsymbol{k}\cdot\tilde{\boldsymbol{A}} - (\hat{\boldsymbol{e}}_2\cdot\boldsymbol{k})(\hat{\boldsymbol{e}}_2\cdot\tilde{\boldsymbol{A}})}{\boldsymbol{k}^2 - (\hat{\boldsymbol{e}}_2\cdot\boldsymbol{k})^2}\, \boldsymbol{k}\, e^{i\boldsymbol{k}\cdot\boldsymbol{x}}\, \frac{d^3k}{(2\pi)^3}, \tag{18}$$

TABLE V: Values of $\langle \boldsymbol{A}^2 \rangle$, $\langle \boldsymbol{A}^2_{\rm 2D} \rangle$, and $\langle \boldsymbol{B}^2 \rangle$ for a low resolution run (144^3 mesh points) and the down-sampled Run A of the Letter (2304^3 mesh points).

resol.	t	$\langle \boldsymbol{A}^2 \rangle$	$\langle \boldsymbol{A}^2_{\rm 2D} \rangle$	$\langle \boldsymbol{B}^2 \rangle$
144^3	10	1.8×10^{-5}	9.7×10^{-6}	1.8×10^{-4}
	50	1.2×10^{-5}	6.0×10^{-6}	8.1×10^{-5}
	100	9.4×10^{-6}	5.1×10^{-6}	4.4×10^{-5}
	200	6.6×10^{-6}	5.0×10^{-6}	2.0×10^{-5}
2304^3	50	5.3×10^{-5}	2.0×10^{-5}	8.2×10^{-4}
	100	4.4×10^{-5}	9.9×10^{-6}	4.0×10^{-4}
	150	4.0×10^{-5}	8.7×10^{-6}	2.6×10^{-4}

In Table V we summarize the values of $\langle \boldsymbol{A}^2 \rangle$ (in the gauge used in the code, i.e., the Weyl gauge) and $\langle \boldsymbol{A}^2_{\rm 2D} \rangle$, and compare their temporal changes with that of $\langle \boldsymbol{B}^2 \rangle$ for a low resolution run and the down-sampled Run A of the Letter. Note first of all that $\langle \boldsymbol{A}^2_{\rm 2D} \rangle$ is always smaller than $\langle \boldsymbol{A}^2 \rangle$. This is expected, because $\boldsymbol{A}$ contains redundant contributions. Second, $\langle \boldsymbol{A}^2_{\rm 2D} \rangle$ decays more slowly than $\langle \boldsymbol{B}^2 \rangle$, demonstrating that $\langle \boldsymbol{A}^2_{\rm 2D} \rangle$ is approximately conserved. Furthermore, the ratio $(\langle \boldsymbol{A}^2_{\rm 2D} \rangle / \langle \boldsymbol{B}^2 \rangle)^{1/2}$ is a length scale of around 0.2 for Run A, which is well above the scale Taylor micro scale shown in Fig. 4 of the Letter. Thus, the typical values of $\langle \boldsymbol{A}^2_{\rm 2D} \rangle$ may well be significant for explaining the $\xi_{\rm M} \sim t^{1/2}$ scaling and its approximate conservation could be responsible for the inverse transfer.

Reynolds and Lundquist numbers

Since $u_{\rm rms}$, $v_{\rm A}$, and k_M are all proportional to $t^{-1/2}$ the decay is self-similar in such a way that the Reynolds and Lundquist numbers, ${\rm Re} = u_{\rm rms}/\nu k_M$ and ${\rm Lu} = v_{\rm A}/\eta k_M$, remain constant. This is clearly demonstrated in Figure 11, where we plot Re (dotted) and Lu (solid) both for Runs A and B with ${\rm Pr}_M = 1$ and 10, respectively.

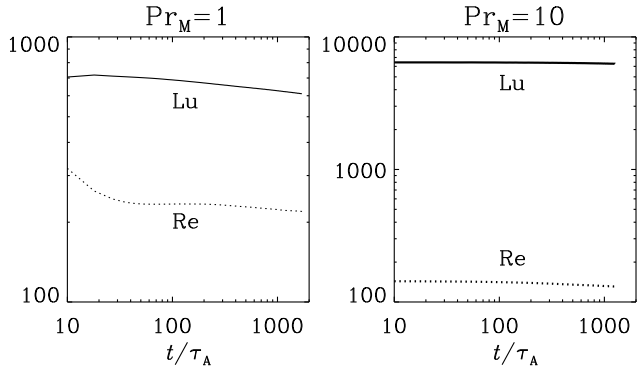

FIG. 11: Instantaneous Reynolds and Lundquist numbers for Runs A and B with ${\rm Pr}_M = 1$ and 10, respectively.

During the decay, the approximate values of Re and Lu are 230 and 700 for Run A and 130 and 6300 for Run B. As discussed in the Letter, for Run B the value of Lu is so huge that, even though we also have a large number of mesh points, one must be concerned about the numerical accuracy of the simulation. One should note, however, that, because ${\rm Pr}_M = 10$ is larger than unity, most of the energy is dissipated viscously. Therefore, although Lu is huge, less magnetic energy needs to be dissipated than for ${\rm Pr}_M = 1$; see Ref. [13] and references therein.

ENERGY TRANSFERS

In the Letter we considered the spectral transfer function $T_{kpq} = \langle \boldsymbol{J}^k \cdot (\boldsymbol{u}^p \times \boldsymbol{B}^q) \rangle$, which governs the gain

of magnetic energy and correspondingly the loss of kinetic energy. There is also a kinetic energy transfer function S_{kpq}, which describes the transfer between different scales. It vanishes for $k = p$ and is given by $S_{kpq} = \rho_0 \langle \boldsymbol{u}^k \cdot (\boldsymbol{u}^p \times \boldsymbol{\omega}^q) \rangle$, where $\rho_0 = \langle \rho \rangle$ is the average density; compressibility effects have been ignored here. The transfer function S_{kpq} enters only in the kinetic energy equation. Thus, the magnetic and kinetic energy equations are given by

$$\frac{d}{dt}\langle \tfrac{1}{2} \boldsymbol{B}_k^2 \rangle = T_{kpq} - \eta k^2 \langle \boldsymbol{B}_k^2 \rangle, \tag{19}$$

$$\frac{d}{dt}\langle \tfrac{1}{2} \rho_0 \boldsymbol{u}_p^2 \rangle = -T_{kpq} - S_{kpq} - \nu p^2 \langle \rho_0 \boldsymbol{u}_p^2 \rangle. \tag{20}$$

Swapping indices k and p in Equation (20) yields

$$\frac{d}{dt}\langle \tfrac{1}{2} \rho_0 \boldsymbol{u}_k^2 \rangle = -T_{pkq} - S_{pkq} - \nu k^2 \langle \rho_0 \boldsymbol{u}_k^2 \rangle. \tag{21}$$

To get the total energy at wavenumber k, we now add Equations (19) and (21), i.e.,

$$\begin{aligned} \tfrac{1}{2} \frac{d}{dt} \langle \boldsymbol{B}_k^2 + \rho_0 \boldsymbol{u}_k^2 \rangle \;=\; & T_{kpq} - T_{pkq} - S_{pkq} \\ & - \eta k^2 \langle \boldsymbol{B}_k^2 \rangle - \nu k^2 \langle \rho_0 \boldsymbol{u}_k^2 \rangle. \end{aligned} \tag{22}$$

The total energy has contributions from all p and q and it is of interest to separate between those that are larger and smaller than k, so we write

$$\begin{aligned} \tfrac{1}{2} \frac{d}{dt} \langle \boldsymbol{B}_k^2 + \rho_0 \boldsymbol{u}_k^2 \rangle \;=\; & \Pi_{p \geq k}^{q \geq k} + \Pi_{p \geq k}^{q < k} + \Pi_{p < k}^{q \geq k} + \Pi_{p < k}^{q < k} \\ & - \eta k^2 \langle \boldsymbol{B}_k^2 \rangle - \nu k^2 \langle \rho_0 \boldsymbol{u}_k^2 \rangle. \end{aligned} \tag{23}$$

where

$$\Pi_{\substack{p > k}}^{\substack{q > k}} = \sum_{\substack{p > k}} \sum_{\substack{q > k}} \left(T_{kpq} - T_{pkq} - S_{pkq} \right). \tag{24}$$

The results in Figure 12 show that $\Pi_{p<k}^{q<k}$ is positive for $k/k_0 > 0.25$, demonstrating that there is a gain of total energy at wavenumbers $k/k_0 > 0.25$ from interactions with smaller wavenumbers. This shows that there is forward transfer at those wavenumbers. Furthermore, for $k/k_0 > 0.25$, the spectral transfer is approximately independent of k, as expected for a proper forward cascade. There is also a short range $0.15 < k/k_0 < 0.3$, where $\Pi_{p>k}^{q<k}$ is negative. This suggests the existence of inverse transfer resulting from mixed interactions of $p > k$ and $q < k$. In our simulations, $|T_{kpq}|$ dominates over $|S_{kpq}|$, so the dominant contribution to wavenumbers q comes from the magnetic field.

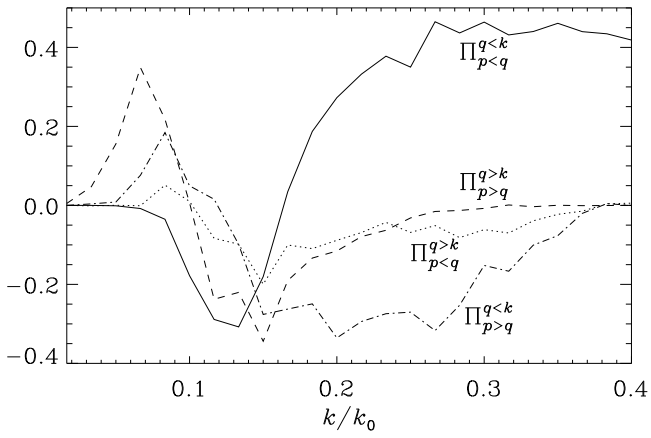

FIG. 12: Energy transfer functions defined in Equation (24).

[1] T. Kahniashvili, A. G. Tevzadze, A. Brandenburg and A. Neronov, Phys. Rev. D **87**, 083007 (2013)
[2] L. Campanelli, Eur. Phys. J. C **74**, 2690 (2014).
[3] P. Olesen, Phys. Lett. B **398**, 321 (1997).
[4] C. Kalelkar and R. Pandit, Phys. Rev. E **69**, 046304 (2004).
[5] M. Christensson, M. Hindmarsh, and A. Brandenburg, Phys. Rev. E **64**, 056405 (2001).
[6] J. Baerenzung, H. Politano, Y. Ponty, and A. Pouquet, Phys. Rev. E **77**, 046303 (2008).
[7] A. Sen, P. D. Mininni, D. Rosenberg, and A. Pouquet, Phys. Rev. E **86**, 036319 (2012).
[8] A. Brandenburg, Å. Nordlund, R. F. Stein, and I. Torkelsson, Astrophys. J. **446**, 741 (1995).
[9] A. Brandenburg, Chaos, Solitons & Fractals **5**, 2025 (1995).
[10] A. Brandenburg, R. L. Jennings, Å. Nordlund, M. Rieutord, R. F. Stein, and I. Tuominen, J. Fluid Mech. **306**, 325 (1996).
[11] S. Sur, L. Pan, and E. Scannapieco, Astrophys. J. **790**, L9 (2014).
[12] A. Pouquet, J. Fluid Mech. **88**, 1 (1978).
[13] A. Brandenburg, Astrophys. J. **791**, 12 (2014).
[14] A. Berera and M. Linkmann, Phys. Rev. E **90**, 041003 (2014).
[15] J. Zrake, Astrophys. J. **794**, L26 (2014).